

---

# CMS Physics Analysis Summary

---

Contact: cms-pog-conveners-pflowtau@cern.ch

2010/07/21

## Commissioning of the Particle-Flow Reconstruction in Minimum-Bias and Jet Events from pp Collisions at 7 TeV

The CMS Collaboration

### Abstract

The first collisions delivered by the Large Hadron Collider at CERN in 2010 are used to commission the CMS particle-flow event-reconstruction algorithm with data taken at a centre-of-mass energy of 7 TeV. The efficient reconstruction and identification of photons, charged and neutral hadrons, made possible by the versatility of the CMS apparatus, are shown to perform as expected up to a high level of precision. Results for particle-based jets and missing transverse energy are shown.



## 1 Introduction

Proton–proton collisions, delivered by the Large Hadron Collider (LHC) at CERN at centre-of-mass energy ( $\sqrt{s}$ ) of 7 TeV, and recorded by the CMS detector [1] during the first half of 2010, are used to validate the particle-flow event reconstruction algorithm, described in Ref. [2] and commissioned at  $\sqrt{s} = 900$  GeV and 2.36 TeV in Ref. [3].

The particle-flow algorithm combines the information from all sub-detectors to identify and reconstruct all particles produced in the collision, namely charged hadrons, photons, neutral hadrons, muons, and electrons. The resulting list of particles can then be used to construct a variety of higher-level objects and observables such as jets, missing transverse energy ( $E_T^{\text{miss}}$ ), taus, lepton and photon isolation, b-jet tagging, etc.

The electron and muon commissioning is presented in Ref. [4]. This note focuses on fully hadronic events. The response of the calorimeter system, important for the reconstruction of photons and neutral hadrons, is studied in Section 2. In Section 3, the cleaning algorithms dealing with anomalous high-energy signals in the calorimeters are described. Finally, the results on particle-based  $E_T^{\text{miss}}$  and jets are presented in Sections 4 and 5, respectively.

The data sample is made of collision events collected with a fully operational detector. It is compared to sample of events generated using PYTHIA 8.135 Tune 1 [5], and simulated using either the Geant-based [6] or the fast simulation [7] of the CMS experiment.

## 2 Calorimeter response to photons and charged hadrons

Electrons and muons aside, the particle-flow algorithm can be roughly summarized in the following way. Tracks reconstructed in the central silicon tracker are extrapolated to the electromagnetic (ECAL) and hadron (HCAL) calorimeter. The charged hadron candidates, in particular their energies and directions, are reconstructed from these tracks. A track is linked to a calorimetric energy cluster in the ECAL and/or in the HCAL if the track extrapolation falls within the boundaries of one of the energy deposits of the cluster. Photons and neutral hadrons are reconstructed from calorimetric energy clusters: clusters separated from the extrapolated position of tracks in the calorimeters constitute a clear signature of these neutral particles; neutral particles overlapping with charged particles in the calorimeters can be detected as calorimeter energy excesses with respect to the sum of the associated track momenta. The photon energy scale is validated in Section 2.1. The response of the calorimeter system to charged hadrons, important both for the detection of overlapping neutral particles and for neutral hadron energy calibration, is studied in Section 2.2.

### 2.1 Calorimeter response to photons

As mentioned above and as described in detail in Ref. [2], photon candidates are reconstructed within the particle-flow algorithm by clustering neighbouring ECAL energy deposits. To reduce the effects of noise, energy thresholds are applied to all ECAL crystals as part of the particle-flow clustering algorithm. Consequently, the energy corresponding to clusters of ECAL crystals is expected to be somewhat smaller than that of the incoming photons, especially at low energy. A residual calibration, determined from simulated single photons, is therefore applied to the cluster energies. The absolute photon-energy calibration was checked using  $\pi^0$ s in a data sample corresponding to an integrated luminosity of  $0.1 \text{ nb}^{-1}$ . To reconstruct  $\pi^0$ s, all photons in the barrel (defined as  $|\eta| < 1.0$  in this paragraph) with an energy of at least 400 MeV were paired. The total photon-pair energy was required to be larger than 1.5 GeV.

The photon-pair invariant-mass distribution is shown in Fig. 1 along with a fit by a Gaussian for the signal, added to an *ad hoc* function for the background. From this fit, an average reconstructed mass of  $135.2 \pm 0.1 \text{ MeV}/c^2$  and a resolution of  $13.2 \pm 0.1 \text{ MeV}/c^2$  are obtained, to be compared with the prediction from the Geant-based simulation of  $136.9 \pm 0.2 \text{ MeV}/c^2$  for the mass and  $12.8 \pm 0.2 \text{ MeV}/c^2$  for the resolution. The agreement with the world average  $\pi^0$  mass of  $135 \text{ MeV}/c^2$  [8] is better than 1%, and the agreement between data and simulation is at the same level. This agreement validates the photon energy scale used in the particle-flow reconstruction algorithm.

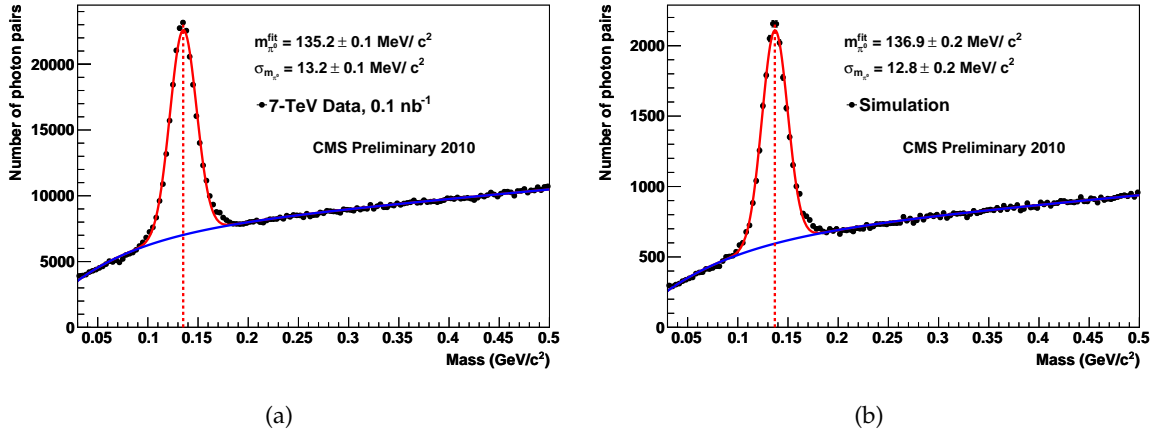


Figure 1: Photon-pair invariant-mass distribution in the barrel ( $|\eta| < 1.0$ ) for the data (a) and the simulation (b).

## 2.2 Calorimeter response to hadrons

A charged or neutral hadron can deposit energy in the electromagnetic calorimeter and in the hadron calorimeter. The hadron energy  $E$  is obtained with a simple linear calibration of the resulting  $E_{\text{ECAL}}$  and  $E_{\text{HCAL}}$  cluster energies [2]. This calibration is essential in the reconstruction of neutral hadrons, but also in the detection of neutral particles overlapping with charged hadrons. The calibration is assumed to be identical for charged and neutral hadrons, and has so far been obtained from single hadrons produced with the fast simulation of the CMS detector.

To verify the calibration procedure, a clean selection of charged hadrons was made in which the charged-hadron candidate was required to have a track with  $p_T > 1 \text{ GeV}/c$ ,  $p > 3 \text{ GeV}/c$  and at least 15 hits, of which at least two in the pixel layers. The requirement on the number of hits was tightened to up to 21 hits when the track points to the end-cap regions, which feature more tracker layers. These stringent criteria are meant to select particles having high-quality tracks with a robust momentum measurement and that reach the calorimeter without experiencing nuclear interactions with the tracker material. The hadron identification was ensured by requiring the track to be linked to a cluster in the hadron calorimeter with  $E_{\text{HCAL}} > 1 \text{ GeV}$ . An isolation requirement was applied by requesting that no other tracks be linked to this cluster, which is loose enough to allow for a very large sample of tracks to be extracted.

Figures 2a and 2b display the average calibrated calorimeter response in the barrel (here defined as  $|\eta| < 1.4$ ) and in the end-caps ( $1.4 < |\eta| < 2.4$ ) for the selected charged hadrons in the data, with a comparison to the raw calorimeter response, as a function of the track momentum. The slope of the cluster calibration curve is close to unity up to the largest energies available so far. Small deviations from unity at low momentum, however, can be observed in

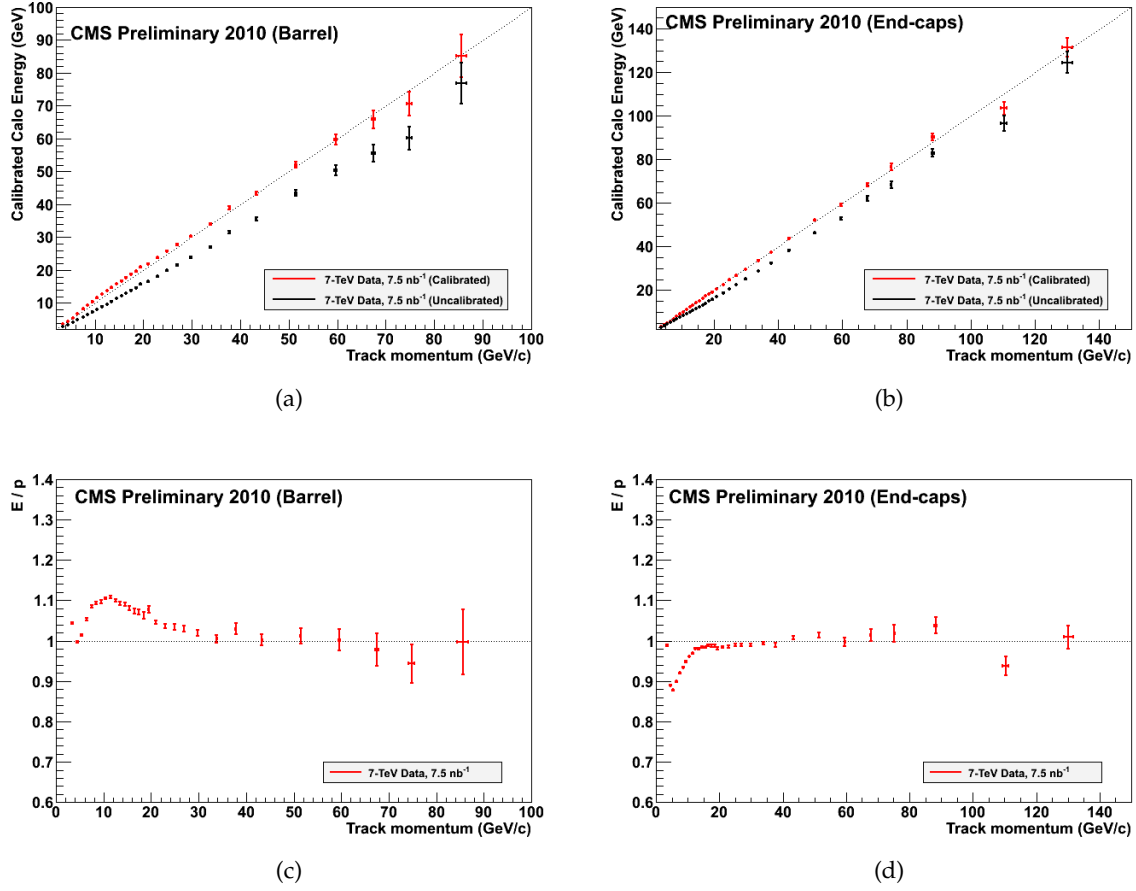


Figure 2: Average raw (black) and calibrated (red) calorimeter response (a,b) and average ratio of the calibrated calorimeter response to the track momentum (c,d) as a function of the track momentum for charged hadrons selected in the data, in (a) the barrel and (b) the end-caps. The diagonal (a,b) and horizontal (c,d) dotted lines indicate the perfect calibration.

Figs. 2c and 2d, which show the mean value of the calibrated calorimeter response divided by the track momentum, as a function of the latter. These small deviations at low momentum may have several origins. A part of them are common to data and simulations, hence are due to the methodology followed here. For example, rare photons and neutral hadrons overlapping with the cluster(s) linked to the track can bias the mean value of  $E/p$  slightly above unity, especially at low momentum. Another part is due to residual differences between data and fast simulation (*e.g.*, difference of  $e/\pi$  response ratio in the ECAL, differences in the calorimeter overall calibration, ...) and will therefore be corrected when the calibration coefficients are determined using the charged hadrons from the data.

The size of the data sample is now sufficient to see, hence to potentially correct, variations of the ratio of the calorimeter response to the track momentum as a function of the latter and of the pseudorapidity of the particle simultaneously, as shown in Fig. 3. The maps are shown separately for minimum-ionizing particles (MIPs) in the ECAL ( $E_{\text{ECAL}} < 0.25$  GeV) and particles interacting in the ECAL ( $E_{\text{ECAL}} > 0.25$  GeV), as they behave differently.

Finally, the ratio of the calorimeter response in the data and the Geant-based simulation is displayed in Fig. 4 in the barrel and the end-caps. Most of the features common to data and simulation disappear from this ratio. The up to 5% larger response in data was identified

to mostly originate from an overcalibration of the hadron calorimeter response in data with respect to the simulation. Because only 15% of the jet energy is carried by neutral hadrons (and because charged hadron energy is measured from the associated track momentum), this moderately larger response in the data translates to a difference in jet-energy scale of about 1 to 2% with respect to the simulation, as demonstrated in Ref. [2]. This small difference will be corrected either with an appropriate determination of the calibration coefficients for the data and the Geant-based simulation separately, and/or with a tuning of the simulation.

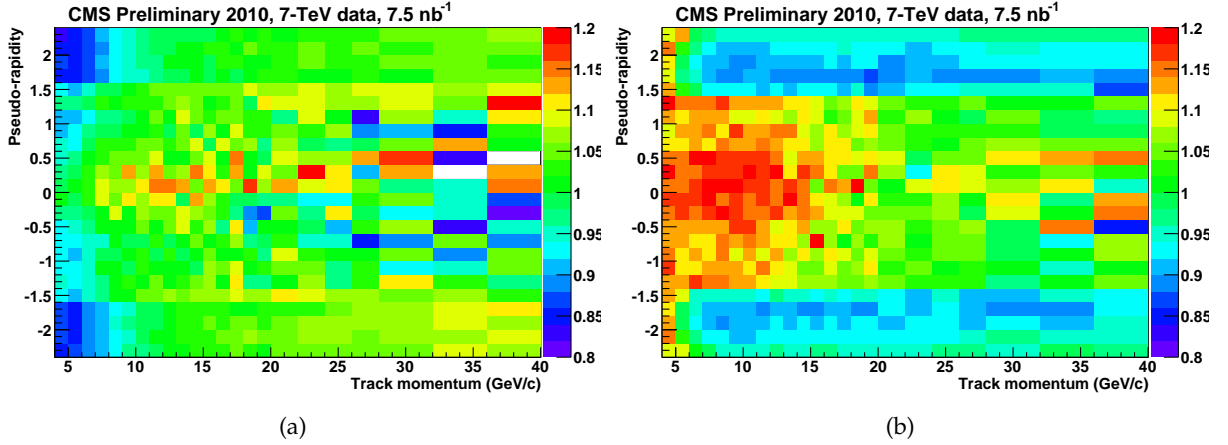


Figure 3: Map of the ratio of the average calibrated calorimeter response to the track momentum as a function of the pseudo-rapidity and the track momentum, for (a) MIPs and (b) particles interacting in the ECAL, for the data.

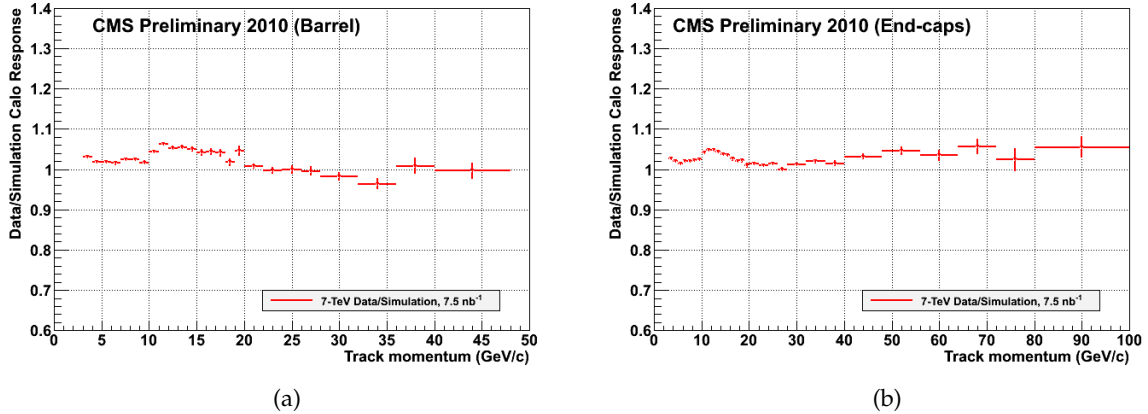


Figure 4: Ratio of the average calibrated calorimeter responses in the data and in the Geant-based simulation as a function of the track momentum for all selected tracks, in (a) the barrel and (b) the end-cap regions.

### 3 Calorimeter-noise cleaning

As was already the case in the 0.9 and 2.36 TeV data, high-energy fake signals were identified in the 7 TeV data, both in individual crystals of the ECAL barrel and in individual towers in the forward hadron calorimeter (HF), in one out of every few hundred events. The rare appearance of coherent noise in the electronics of the HCAL [9], such as discharges in the hybrid photodiodes (HPD) affecting blocks of up to 18 cells at the same  $\phi$  values, or global pedestal

drifting in read-out boxes (RBX) affecting up to four adjacent HPDs, was also confirmed in the recent collision data. The existence of this high-energy calorimeter noise can cause the particle-flow algorithm to reconstruct fake neutral particles, ultimately leading to significant fake missing transverse energy. The effects of the noise cleaning was therefore evaluated with the  $E_T^{\text{miss}}$  distribution in a sample of about 100 million minimum-bias events recorded at 7 TeV, corresponding to an integrated luminosity of about  $7.5 \text{ nb}^{-1}$ .

Substantial progress had already been achieved in cleaning such noise effects with 200 000 events recorded at lower centre-of-mass energies [3], by rejecting from further processing (i) high-energy deposits in single ECAL crystals surrounded by no or little energy in the four neighbouring crystals; (ii) high-energy deposits in HF short fibres, not backed up by some energy in the long fibres of the same HF tower; (iii) high-energy deposits in HF long fibres surrounded by no or little energy in the short fibres of the same HF tower and in the short and long fibres of the four neighbouring HF towers; and (iv) high-energy deposits in large groups of HCAL towers from a single HPD or RBX. As the simulation used for this work did not yet include these anomalous features, the rejection criteria were tuned to reject no single crystal, HCAL tower or HF tower from large simulated samples of minimum-bias events, QCD events with hard-scattering transverse momentum,  $\hat{p}_T$ , up to  $3 \text{ TeV}/c$ , and isolated energetic photons.

Because of the increased statistics and larger occupancy, many spurious high-energy deposits were found not to be cleaned in the 7-TeV collisions by the procedure developed in 2009, and new strategies had to be developed. For ECAL crystals, it was noticed that the vast majority of the spurious deposits are not in phase with the beam crossing (i.e., either late or ahead of time) [10]. It was therefore requested, for all deposits in excess of  $2 \text{ GeV}$ , that the measured time be within  $\pm 5\sigma$  (typically a few ns) of the expected time [10]. Similarly, the measured time of HF deposits in excess of  $30 \text{ GeV}$  was required to be within  $\pm 5 \text{ ns}$  of the expected time, and the time distribution was required to be compatible with that expected from a real energy deposit originating from the collision debris. Finally, deposits in HF long fibres in excess of  $120 \text{ GeV}$ , not backed up by at least 1% of the long-fibre energy in the short fibres of the same HF tower, were rejected.

Because the HF timing and long-fibre requirements are known to occasionally reject some real signal (for example, energetic photons may leave energy solely in long fibres, in about 0.1% of the cases), an *a posteriori* recovery algorithm was implemented: when the cleaning of an HF channel was found to be responsible for more than half of the total missing transverse energy in an event, this deposit was included back in the list of reconstructed particles. This procedure is invoked in less than 0.1% of the events, and prevents the bulk of the events, with no true missing transverse energy, from polluting the sample of rare events with large missing transverse energy. The recovery procedure is successful in the majority of the simulated events with a cleaned transverse energy in excess of  $5 \text{ GeV}$ . For the 0.1% of the events with true missing transverse energy for which it would be invoked, the procedure is ineffective, and has therefore no bias towards small missing transverse energies, as it would require a double coincidence (in magnitude and in direction) between the cleaned transverse energy in one single HF channel and the true transverse missing energy.

The effect of the cleaning procedure is displayed in Fig. 5, in which the missing-transverse-energy distribution is displayed at different cleaning stages. Starting from the top curve, the inclusive raw distribution, without any calorimeter-noise cleaning attempted and with a very loose event selection, exhibits a peak at around  $280 \text{ GeV}$ . This peak corresponds to a single  $5 \times 5$  crystal area in the ECAL that detected the laser calibration signal from the previous (empty) bunch crossing. In a first, global, cleaning stage, this short data taking period was declared a

“bad run” (i.e., not useable for analysis) by the data-certification team. By using only runs certified for data analysis (“good runs”), the peak disappears as seen from the second distribution in this figure. Beside validating a posteriori the data-certification procedure, this distribution shows that, considering the early state of detector operations, a very large fraction of all collected data is certifiably good quality. The effect of the topological cleaning developed for the 2009 data is shown in the third distribution, for which the tail is reduced by several orders of magnitude. Finally, the fourth, cleanest, distribution includes the use of timing information, added in the 2010 cleaning version.

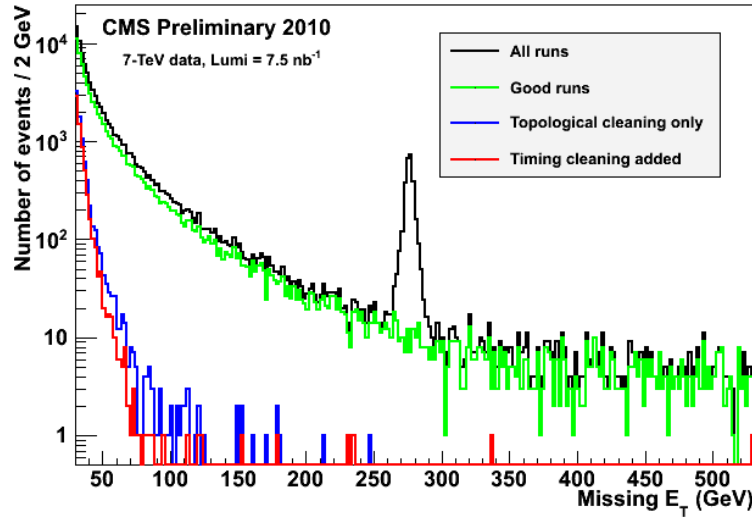


Figure 5: Distributions of missing transverse energy above 30 GeV, for 100 million collisions recorded at 7 TeV. From top to bottom: before any cleaning (black); for the subset of these collisions in the “good runs” (green); with the topological cleaning applied (blue); and with the timing cleaning procedure included (red). Most events with a missing transverse energy larger than 30 GeV before cleaning move off scale (below 30 GeV) after cleaning.

With this upgraded cleaning algorithm, the numbers of events with a missing transverse energy in excess of 40, 60 and 80 GeV were found to be 556, 46 and 13 respectively, to be compared to 925, 137 and 56 with the 2009 version. (The missing transverse energy distributions shown in the next section feature less events, as they include additional requirements on the trigger and on the reconstructed primary vertex.) A visual inspection of the 13 events with a reconstructed missing transverse energy in excess of 80 GeV was performed. Seven of them were found to be due to residual noise in the calorimeters (five in the HCAL, two in the HF), which the present cleaning algorithms were not able to identify. The new cleaning strategy therefore allowed the calorimeter noise to be reduced by almost yet another order of magnitude with respect to the topological cleaning developed for the 2009 data. Among the six other events, four have a forward muon reconstructed with very large transverse momentum (532, 344, 238 and 83 GeV/c), due to a poor reconstruction of the associated track in the central tracker. The reasons of the poor track reconstruction are being investigated. No obvious reasons could be found for the remaining two events, in which the missing transverse energy thus comes from either neutrinos or current algorithmic limitations. No obvious reasons could be found either for more than half of the 30 events with a missing transverse energy between 60 and 80 GeV. This observation shows that calorimeter noise no longer dominates the tail of the distribution, now pretty well described by the simulation (Section 4).



## 4 Missing Transverse Energy

The missing transverse energy vector is computed as the opposite of the transverse-momentum sum of all particles reconstructed in the event. The modulus of this vector is the missing transverse energy  $E_T^{\text{miss}}$  and its projections on the  $x$  and  $y$  axes are denoted  $E_x^{\text{miss}}$  and  $E_y^{\text{miss}}$ , respectively. Minimum-bias collisions and QCD multi-jet events are expected to be momentum balanced in the plane transverse to the beam axis, and so have zero or little  $E_T^{\text{miss}}$ . Samples of such events therefore provide an excellent laboratory for testing the effects of the calorimeter-noise cleaning procedure described in Section 3, as well as studying the response and resolution of the global event description from the particle-flow reconstruction up to the highest energy collisions and momentum transfers.

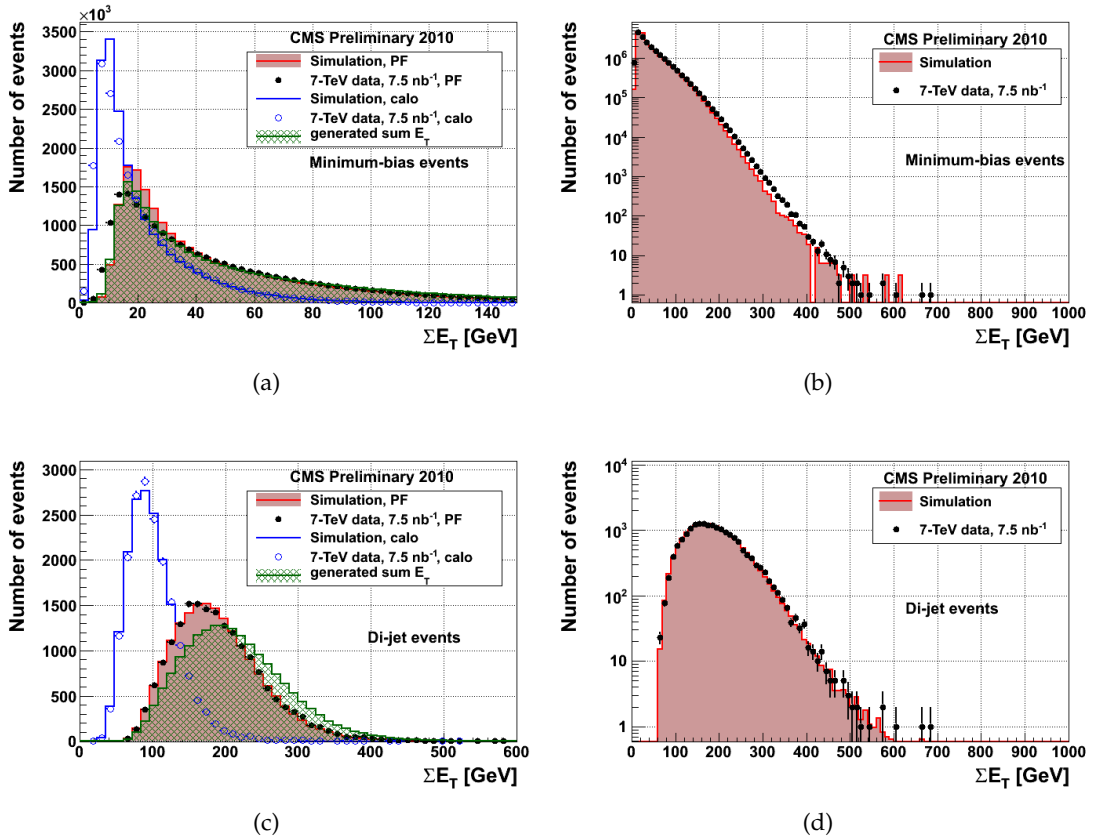


Figure 6: Distribution of the calorimeter-based (hollow) and particle-based (solid)  $\Sigma E_T$  in the data (dots) and in the simulation (histogram) for (a,c) linear scale and (b,d) log scale for (top) minimum-bias collisions and (bottom) di-jet events. In (a,c), the distributions of the true  $\Sigma E_T$  are also shown for the simulated events.

The total visible transverse energy of an event is computed as the scalar sum of the transverse energies of all reconstructed particles and denoted  $\Sigma E_T$ . This observable is particularly sensitive to the modelling of both the underlying event in the generator, and the calorimeter noise in the simulation. The results presented here are based on two different samples. The first sample corresponds to minimum-bias collisions and allows performance studies at low  $\Sigma E_T$ . The generator is however known to be inaccurate in this non-perturbative QCD regime. The second sample corresponds to di-jet events, selected by requiring at least two jets with a corrected  $p_T$  [11] in excess of 25 GeV/c. This sample allows the simulation to mostly rely on perturba-

tive QCD, and is closer to the phase space in which  $E_T^{\text{miss}}$  in hadronic events is expected to be used. All distributions presented hereafter are produced after the cleaning procedure described in Section 3, and with an integrated luminosity of  $7.5 \text{ nb}^{-1}$ . In addition to Section 3, a well-defined primary vertex and a basic minimum-bias trigger are required.

The distributions of the particle-based  $\sum E_T$  and the calorimeter-based  $\sum E_T$  are compared to the generated  $\sum E_T$  in Fig. 6. On average, the particle-based  $\sum E_T$  reconstructs 80% of the true  $\sum E_T$ , twice as much as the calorimeter-based  $\sum E_T$ . On the one hand, Fig. 6b demonstrates that simulated minimum-bias collisions contain slightly less  $\sum E_T$  than in the data. On the other hand, Fig. 6d shows that once a di-jet sample is selected, favouring a perturbative QCD description of the event, the simulation and data agree, up to the highest  $\sum E_T$  values.

The distribution of the particle-based  $E_T^{\text{miss}}$  is shown in Figs. 7a and 7b. The number of events with  $E_T^{\text{miss}} > 5 \text{ GeV}$  is smaller in simulated minimum-bias collisions than in the data, which is consistent with the smaller generated event activity, visible in Fig. 6b. In the case of di-jet events (Figs. 7c and 7d) a better agreement is obtained. The residual excess of  $E_T^{\text{miss}}$  in the data has been shown to be due to the reconstructed neutral hadrons, affected by the higher hadron calorimeter response observed in the data (Section 2.2), as shown in Figure 4. When a data-driven calorimeter calibration is available, this excess is expected to disappear.

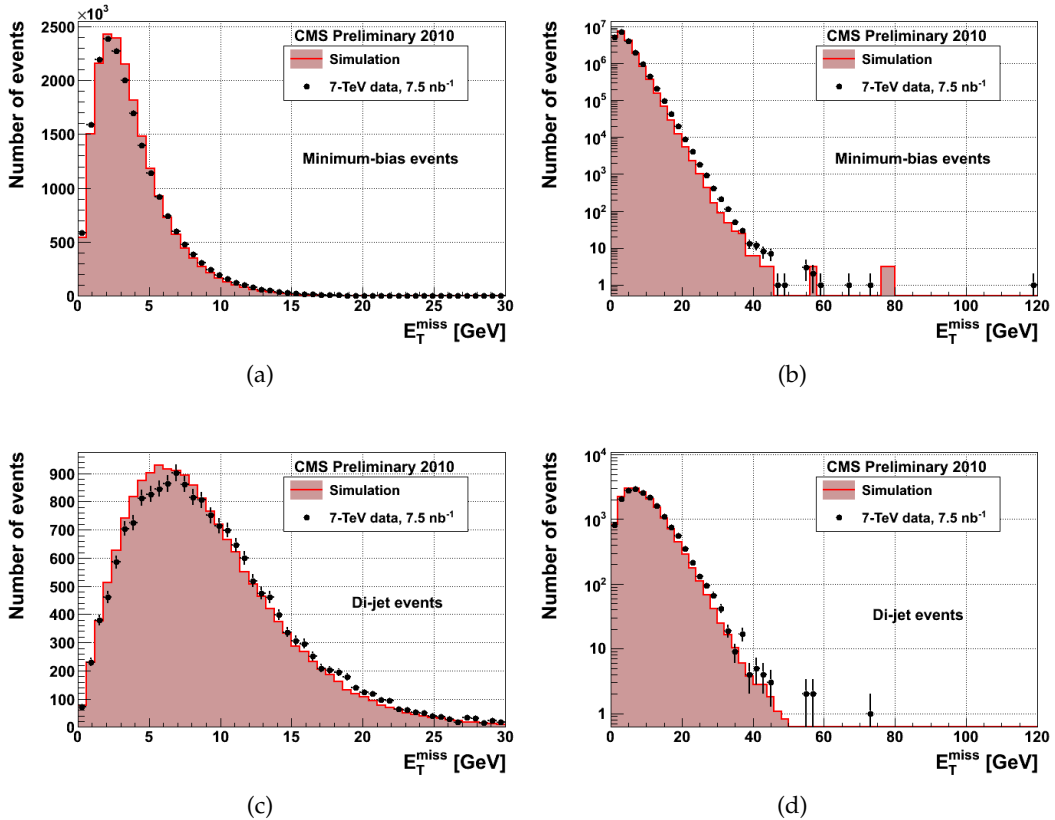


Figure 7: Distribution of  $E_T^{\text{miss}}$  in data (dots) and simulation (histogram) for minimum-bias collisions (top) and di-jet events (bottom) in (a,c) linear scale and (b,d) logarithmic scale.

The measured  $\sum E_T$  of an event sets a natural scale by which to gauge the performance of the measured  $E_T^{\text{miss}}$ . The relative accuracy with which a nil missing transverse energy is reconstructed, *i.e.*, the ratio  $E_T^{\text{miss}} / \sum E_T$ , is displayed in Figs. 8a and 8b for events with  $\sum E_T > 3 \text{ GeV}$

in the case of minimum-bias collisions and effectively  $\sum E_T > 50$  GeV in the case of di-jet events. Particle-flow improves this relative  $E_T^{\text{miss}}$  reconstruction accuracy by a factor two with respect to the traditional calorimeter-based technique.

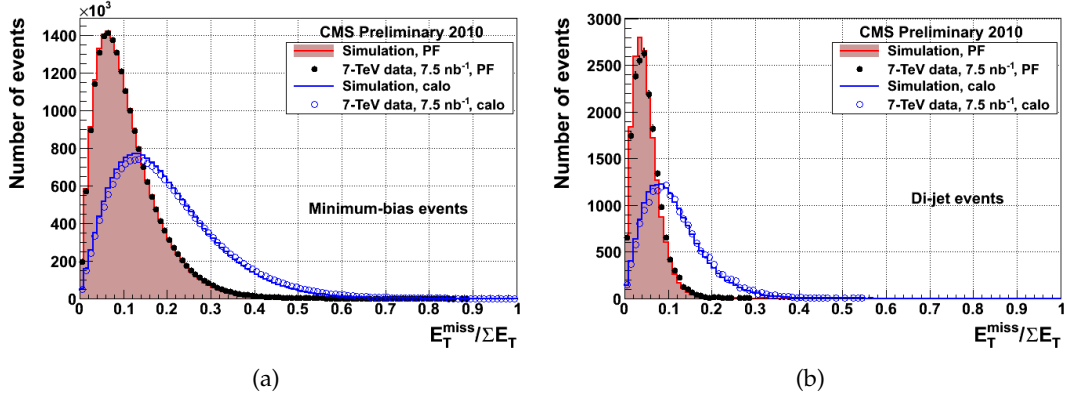


Figure 8: Distribution of the particle-based (solid) and calorimeter-based (hollow) relative  $E_T^{\text{miss}}$  resolution,  $E_T^{\text{miss}} / \sum E_T$ , in data (dots) and simulation (histogram), (a) in minimum-bias collisions and (b) di-jet events.

The improved  $E_T^{\text{miss}}$  resolution can also be visualized as a function of  $\sum E_T$ . The distribution of  $E_x^{\text{miss}}$  and  $E_y^{\text{miss}}$  was fit to a Gaussian, for several bins of  $\sum E_T$ . The resulting width  $\sigma(E_{x,y}^{\text{miss}})$  is shown as a function of the particle-based  $\sum E_T$  in Fig. 9a for the minimum-bias sample, and in Fig. 9b for the di-jet sample. The particle-based  $E_T^{\text{miss}}$  and  $\sum E_T$  were corrected for the jet energy scale of particle-based jets with a raw  $p_T > 1$  GeV/c. The calorimeter-based  $E_T^{\text{miss}}$ , corrected for the jet energy scale of calorimeter-based jets with corrected  $p_T > 20$  GeV/c, and for low- $p_T$  effects [12], is also shown as a function of the particle-based  $\sum E_T$ . The factor two improvement in resolution for particle-based  $E_T^{\text{miss}}$  is confirmed in Ref. [12]. The stochastic term driving the evolution with  $\sum E_T$  of the particle-based  $E_x^{\text{miss}}$  and  $E_y^{\text{miss}}$  resolution is between 50% and 60%.

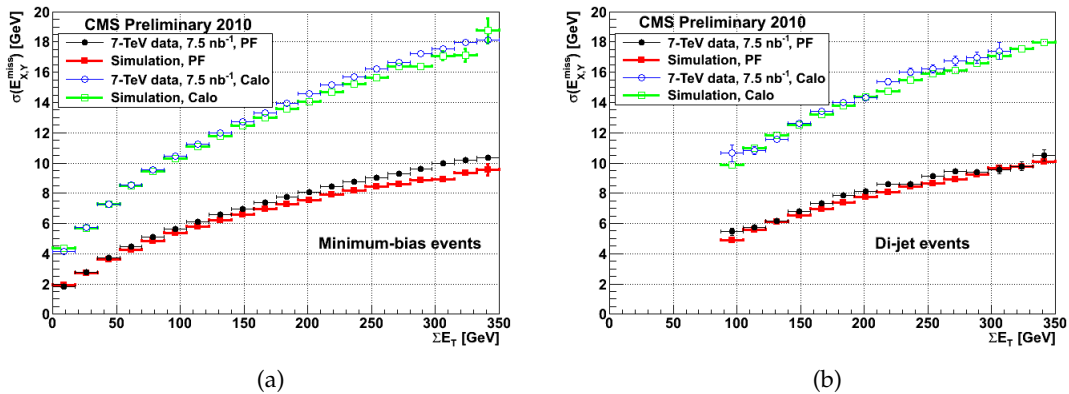


Figure 9: Resolution of  $E_{x,y}^{\text{miss}}$  for particle-based (solid symbols) and calorimeter-based (hollow symbols) reconstruction in data (dots) and simulation (squares), as a function of the particle-based  $\sum E_T$ , for (a) minimum-bias collisions; and (b) di-jet events. The particle-based  $E_T^{\text{miss}}$  and  $\sum E_T$  are corrected for the jet energy scale of particle-based jets and the calorimeter-based  $E_T^{\text{miss}}$  is corrected for both the jet energy scale of calorimeter-based jets (with corrected  $p_T > 20$  GeV/c) as well as low- $p_T$  effects.

## 5 Jets

The expected jet resolution and response, as well as a first attempt at a measurement of these quantities are presented in Ref. [11]. The present study focuses on commissioning the composition of jets made of reconstructed particles. All particles were clustered into jets with the anti- $k_T$  algorithm [13], with distance parameter  $R = 0.5$ . Residual jet energy scale corrections, of the order of 5% in the barrel and 10% in the end-caps, obtained from the simulation, were then applied to reach unit response. Di-jet events were selected by requiring a basic minimum-bias trigger together with a well-defined primary vertex, in a sample corresponding to an integrated luminosity of  $6.2 \text{ nb}^{-1}$ . All distributions are presented after the cleaning procedure described in Section 3 has been applied. Additionally, a di-jet sample was formed by requiring the two jets to be well contained in the detector acceptance ( $|\eta| < 3$ ), to be back-to-back (opening azimuthal angle greater than  $\pi - 0.5$ ), and to have a transverse momentum  $p_T$  in excess of  $25 \text{ GeV}/c$ . All jets satisfying those criteria were considered. No jet quality criteria were applied, for a maximum sensitivity to possible detector effects.

Basic jet properties (transverse momentum, invariant mass, ratio of jet momentum to jet invariant mass, angular position, and constituent multiplicity) are presented in Fig. 10, which shows the level of agreement between data and simulation.

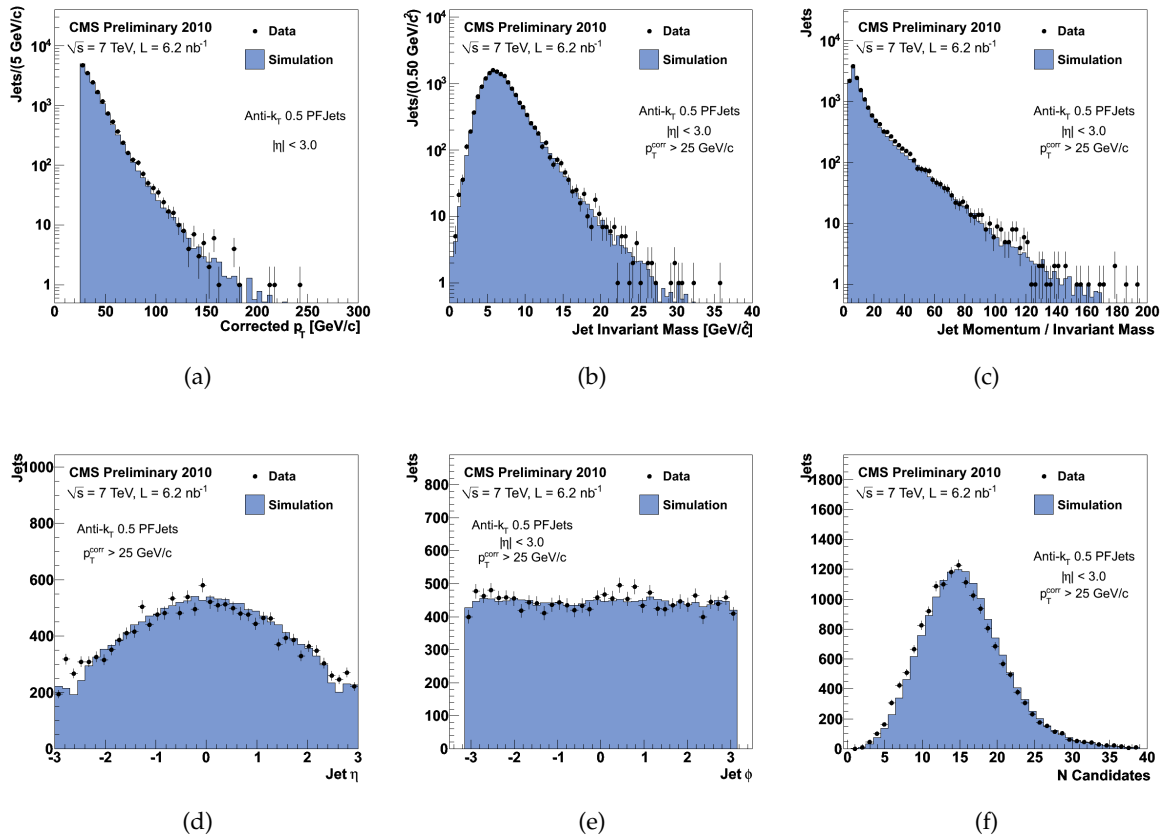


Figure 10: Basic jet properties in di-jet events: Distributions of (a) jet transverse momentum; (b) jet invariant mass; (c) the ratio of jet momentum to jet invariant mass; (d) jet pseudorapidity; (e) jet azimuth; and (f) number of particle constituents in a jet.

The most significant deviation appears as an excess of jets beyond the tracker acceptance ( $|\eta| > 2.5$ ). This excess is the combined result of the slightly larger response of the hadron

calorimeter in the data (Section 2.2), which affects both neutral and charged hadrons in the region not covered by the tracker, and of the jet  $p_T$  cut applied to a steeply falling spectrum. The next-to-most-significant deviation is a half-a-unit shift in the distribution of the number of jet constituents. As this variable is sensitive to the details of the fragmentation modelling, such a small deviation can actually be seen as a remarkable achievement.

The jet constituent particles were classified into seven types: charged hadrons, photons, neutral hadrons, electrons, muons, and electromagnetic and hadronic energy deposits in the HF. For each reconstructed jet, the jet-component energy  $E_X$  is the total energy carried by the particles of type  $X$  contained in this jet, and the jet energy fraction  $R_X$  is the fraction of the jet energy carried by the particles of type  $X$ ,  $R_X = E_X / E_{\text{jet}}$ . Figures 11a and 11b show the mean jet energy fractions for the various particle types across detector boundaries. In the tracker-covered region, charged hadrons were found to carry on average 65% of the jet energy, photons 25% and neutral hadrons 10%. The capability of the forward calorimeter to separate the electromagnetic and hadronic energy deposits is not yet exploited in the particle-flow algorithm, and studies show that the fraction of hadronic energy observed in reconstructed jets is currently overestimated, both in the data and in the simulation.

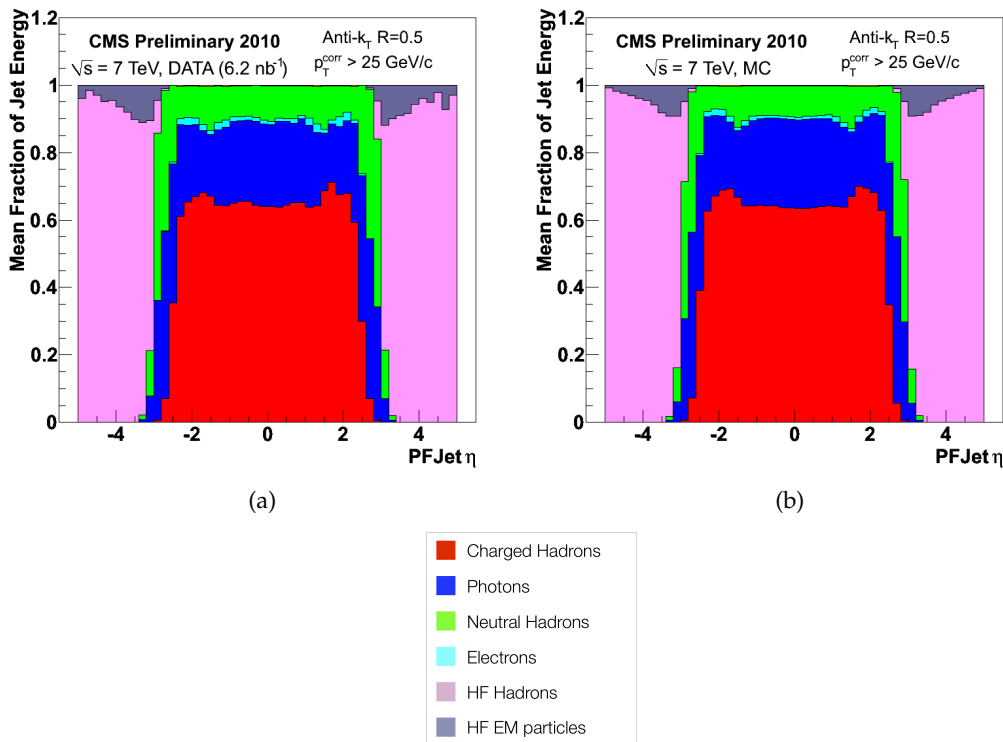


Figure 11: Reconstructed jet energy fractions as a function of pseudorapidity (a) in the data (b) and in the simulation. From bottom to top in the central region: charged hadrons, photons, electrons, and neutral hadrons. In the forward regions: hadronic deposits, electromagnetic deposits.

The distributions of the jet-component energies for charged hadrons, photons, and neutral hadrons are shown in Fig. 12, separately in the barrel and in the end-caps. The small, but visible discrepancy in the neutral-hadron-fraction distributions, especially in the endcaps, is yet another manifestation of the over-calibration of the hadron calorimeter in the data with respect to the simulation.

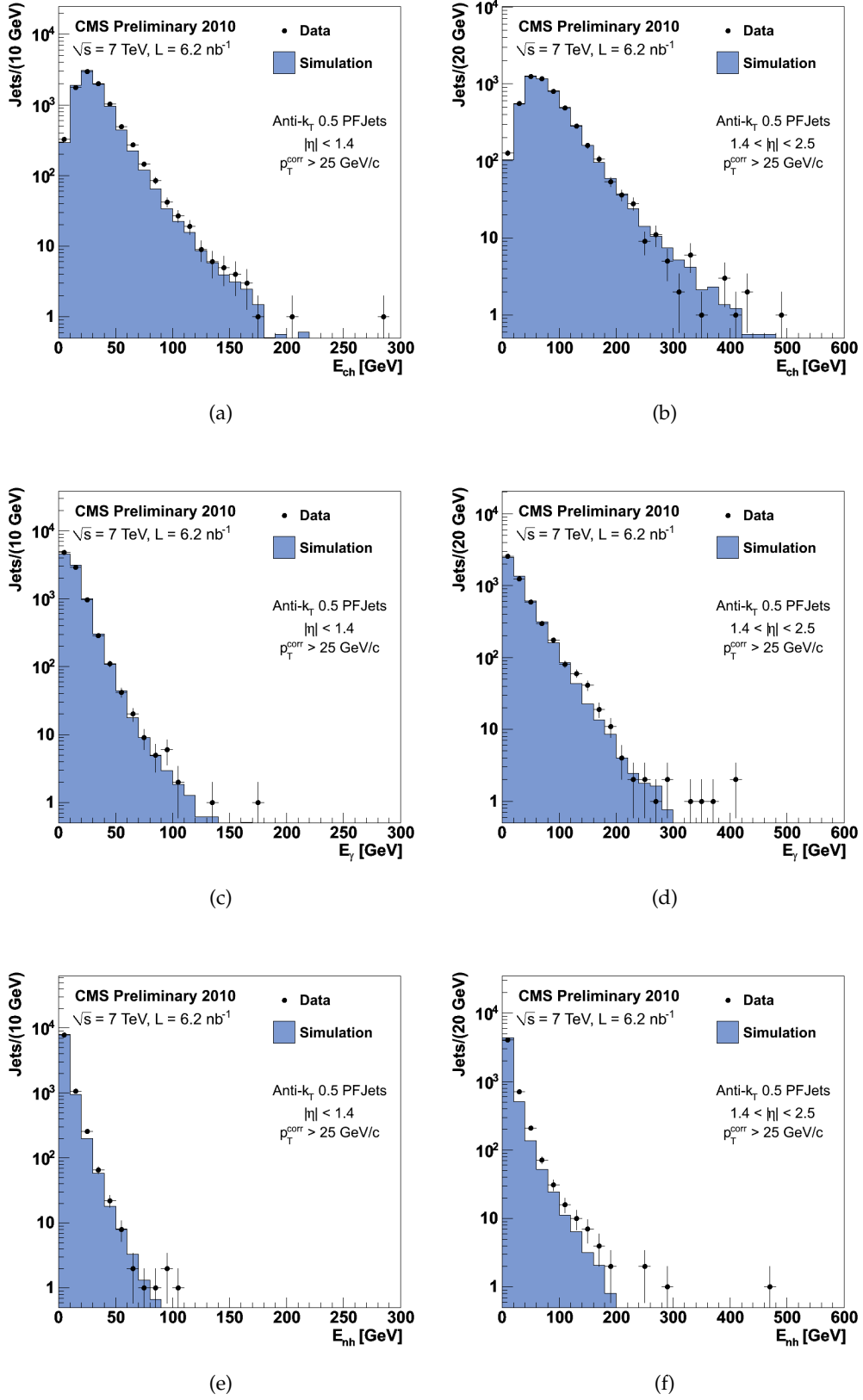


Figure 12: Component of the jet energy carried by charged hadrons (a,b), photons (c,d) and neutral hadrons (e,f), in the barrel (left) and in the end-caps (right).

## 6 Conclusion

Progress on further commissioning the particle-flow event reconstruction has been made using the early 7-TeV proton–proton collision data, provided by the Large Hadron Collider and recorded by the CMS detector during the first half of 2010. The photon energy-scale calibration has been verified to within one per cent, with reconstructed  $\pi^0$ s. While work is still in progress to derive a full calibration for the hadron energy scale, the calibration has already been verified to be accurate to within a per cent at high transverse energy, using high momentum tracks up to 100 GeV/ $c$  in the barrel and 150 GeV/ $c$  in the end-caps. The 5%-level deviations observed at low momentum point to the need of a residual calibration of the hadron calorimeter response. Calorimeter noise has been further studied and the cleaning refined, resulting in one spurious hit having transverse energy above 50 GeV per  $3 \times 10^6$  events. Results for particle-based jets and missing transverse energy have also been presented. The simulation has been shown to be in good agreement with the data for QCD di-jet events, both for the observed jets and  $E_T^{\text{miss}}$  spectra as well as the particle composition.

## References

- [1] CMS Collaboration, “The CMS experiment at the CERN LHC”, *JINST* **0803** (2008) S08004. doi:10.1088/1748-0221/3/08/S08004.
- [2] CMS Collaboration, “Particle-Flow Event Reconstruction in CMS and Performance for Jets, Taus, and Missing  $E_T$ ”, *CMS PAS PFT-09-001* (2009).
- [3] CMS Collaboration, “Commissioning of the Particle-Flow Event Reconstruction with the First LHC collisions recorded in the CMS detector”, *CMS PAS PFT-10-001* (2010).
- [4] CMS Collaboration, “Particle-flow commissioning with muons and electrons from J/Psi, and W events at 7 TeV”, *CMS PAS PFT-10-003* (2010).
- [5] T. Sjostrand, S. Mrenna, and P. Z. Skands, “A Brief Introduction to PYTHIA 8.1”, *Comput. Phys. Commun.* **178** (2008) 852–867, arXiv:0710.3820. doi:10.1016/j.cpc.2008.01.036.
- [6] S. Agostinelli, J. Allison, K. Amako et al., “G4—a simulation toolkit”, *Nuclear Instruments and Methods in Physics Research Section A: Accelerators, Spectrometers, Detectors and Associated Equipment* **506** (2003), no. 3, 250 – 303. doi:10.1016/S0168-9002(03)01368-8.
- [7] CMS Collaboration, “CMS: Detector Performance and Software”, *CERN/LHC 2006-001* (2006).
- [8] Particle Data Group Collaboration, “Review of particle physics”, *Phys. Lett.* **B592** (2004) 1. doi:10.1016/j.physletb.2004.06.001.
- [9] CMS Collaboration, “Identification and Filtering of Uncharacteristic Noise in the CMS Hadron Calorimeter”, arXiv:0911.4881.
- [10] CMS Collaboration, “Electromagnetic calorimeter commissioning and first results with 7 TeV data”, *CMS Note* **2010/012** (2010).
- [11] CMS Collaboration, “Jet Performance in pp Collisions at  $\sqrt{s} = 7$  TeV”, *CMS PAS JME-10-003* (2010).

- [12] CMS Collaboration, “MET Performance in Minimum-Bias and Jet Events from pp Collisions at  $\sqrt{s} = 7$  TeV”, *CMS PAS JME-10-004* (2010).
- [13] M. Cacciari, G. P. Salam, and G. Soyez, “The anti-kt jet clustering algorithm”, *JHEP* **04** (2008) 063, [arXiv:0802.1189](#).